

Outlier Accommodation for GNSS Precise Point Positioning using Risk-Averse State Estimation

Wang Hu, Jean-Bernard Uwineza, and Jay A. Farrell

Abstract—Reliable and precise absolute positioning is necessary in the realm of Connected Automated Vehicles (CAV). Global Navigation Satellite Systems (GNSS) provides the foundation for absolute positioning. Recently enhanced Precise Point Positioning (PPP) technology now offers corrections for GNSS on a global scale, with the potential to achieve accuracy suitable for real-time CAV applications. However, in obstructed sky conditions, GNSS signals are often affected by outliers; therefore, addressing outliers is crucial. In GNSS applications, there are many more measurements available than are required to meet the specification. Therefore, measurement selection is important to avoid outlier measurements is of interest. The recently developed Risk-Averse Performance-Specified (RAPS) state estimation optimally selects measurements to minimize outlier risk while meeting a positive semi-definite constraint on performance; at present, the existing solution methods are not suitable for real-time computation and have not been demonstrated using challenging real-world data or in Real-time PPP (RT-PPP) applications. This article makes contributions in a few directions. First, it uses a diagonal performance specification, which reduces computational costs relative to the positive semi-definite constraint. Second, this article considers GNSS RT-PPP applications. Third, the experiments use real-world GNSS data collected in challenging environments. The RT-PPP experimental results show that among the compared methods: all achieve comparable performance in open-sky conditions, and all exceed the Society of Automotive Engineers (SAE) specification; however, in challenging environments, the diagonal RAPS approach shows improvement of 6-19% over traditional methods. Throughout, RAPS achieves the lowest estimation risk.

I. INTRODUCTION

Reliable and accurate real-time positioning is crucial for CAV within the framework of intelligent transportation systems [1], [2]. The widespread adoption of CAV holds promise to alleviate congestion, decrease both the frequency and severity of accidents, reduce emissions, enhance system resilience by addressing bottlenecks, and offer numerous other benefits [3]. Precise and dependable localization and positioning are fundamental requirements for CAV applications [1], [4]. Accurate absolute positioning is facilitated by GNSS. For CAV applications, the SAE J2945 specification defines the requirement for horizontal and vertical position errors to be less than 1.5 m and 3.0 m, respectively, with a probability of 68% [5]. However, standalone GNSS receivers, when not supplemented with external corrections, usually achieve positioning accuracy around 10 meters [6]. This limitation is caused by common-mode errors (CME) in GNSS measurements [7], [8].

W. Hu (whu027@ucr.edu), J.- B. Uwineza (juwin001@ucr.edu), and J. A. Farrell (farrell@ece.ucr.edu) are with the Dept. of Electrical and Computer Engineering, U. of California, Riverside, CA 92521, USA.

Early and traditional methods to counteract the effects of CME employed observation space representation corrections. This approach is commonly associated with Differential GNSS (DGNSS), where receivers acquire lumped CME corrections either from a processing center or nearby base stations. DGNSS using pseudorange measurements typically yields an accuracy within the range of 1-3 meters. In contrast, DGNSS using phase measurements (often referred to as Real-time Kinematic Positioning (RTK)) can attain centimeter-level accuracy when integer ambiguities are correctly resolved [8]. However, these DGNSS advantages necessitate extensive local base station infrastructure and do not inherently provide corrections with global coverage.

The PPP corrections have global applicability without the need for users to access local base stations; therefore, they are more appropriate for applications such as CAV that require global coverage. PPP uses state space representation, which utilizes models for each individual components of the CME [9]. These methods were originally developed for post-processing in GPS surveying applications. The International GNSS Service (IGS) Multi-GNSS Experiment (MGEX) project is a global collaboration, involving Centre National d'Études Spatiales (CNES), Wuhan University (WHU), Chinese Academy of Sciences (CAS), German Aerospace Center (DLR), and others agencies, to compute and communicate globally relevant RT-PPP corrections with low latency (approximately 10 seconds) for multi-GNSS systems (e.g., GPS, GLONASS, Galileo, BeiDou). Its products have recently advanced to the point where they are suitable for real-time GNSS operations [9], [10].

Each satellite system is designed to provide visibility of 6-12 satellites at any given epoch. Each satellite provides measurements on more than one frequency and signal. Leveraging multiple GNSS systems, frequencies, and signals provides significantly more measurements than the four spatially diverse satellite measurements that are the theoretical requirement for a position (and clock) solution and often more than required to meet the stated accuracy specification. When the number of measurements is high, all measurements are outlier-free, and their accuracy is known, utilizing all measurements with optimal state estimation would yield accuracy that far surpasses the requirements of the J2945 specification.

GNSS measurements are impacted by multipath and non-line-of-sight effects, as well as spoofing, which can have large-magnitude effects. While multipath and non-line-of-sight errors tend to be small under open sky conditions [11], they become pronounced in challenging environments,

such as urban areas (e.g., narrow lanes surrounded by tall buildings and trees). In such settings, GNSS signals, due to various reflections, are prone to substantial multipath errors. Using these outliers measurements within state estimation can distort the state estimate, resulting in over-confidence (i.e., too small covariance) in an incorrect estimate. The traditional methods to accommodate outliers in state estimation evaluate measurement residuals using fixed or adaptive thresholds [12]–[14]. In other applications, such as least squares, additional outlier rejection methods have been explored, including least soft-threshold squares [15] and median least squares [16]. These approaches primarily aim to detect and disregard outliers or to de-weight measurements based on the magnitude of their residuals. These approaches may far surpass the specification requirements when many outlier-free measurements are available and may not meet the performance specification in circumstances where many measurements are de-weighted or removed. They do not have a mechanism to balance between minimizing measurement risks and satisfying performance specifications.

An alternative optimization-based approach that selects a subset of measurements to achieve a performance specification constraint while minimizing risk is introduced as RAPS estimation in [17]–[19]. The RAPS optimization problem under study necessitates that the performance specification constraint be positive semi-definite. An alternative method, employing a diagonal performance specification, has been mentioned but has not yet been evaluated. A diagonal performance specification eliminates the computational overhead associated with verifying the positive definiteness of a matrix, which has a time complexity of $O(n^3)$ in every step of searching for the measurement selection vector in each epoch. In addition, prior research showcased RAPS within the context of DGNSS with artificially imposed outliers. RAPS has not yet been evaluated in cutting-edge RT-PPP applications or using real-world GNSS data acquired in challenging environments.

Many legacy and low-cost receivers that are currently typical in automotive applications typically only support single frequency. Single frequency GNSS measurement types include pseudorange, carrier phase, and Doppler. The advantages of utilizing phase measurements hinge on the accurate mitigation of CME and correct estimation of integer ambiguities. When outliers are present, GNSS carrier phase measurements become susceptible to outages and cycle slips that complicate ambiguity estimation. Furthermore, phase measurement-based PPP-RTK demands enhanced corrections for atmospheric delays, necessitating slant Total Electron Content (TEC) and tropospheric messages. These are expected in the third stage scheduled by IGS, which is currently only in its second stage [9].

This paper’s contribution lies in demonstrating outlier accommodation for multi-GNSS single frequency RT-PPP, focusing on pseudorange and Doppler, using a diagonal performance-specified RAPS approach. The experiments use real-world data. This paper is structured as follows. Section II reviews the GNSS observation models for pseudorange

and Doppler. Section III discusses the RT-PPP sources and models for mitigating the CME. Section IV compares the RAPS and Threshold Decisions (TD) approaches in state estimation. Section VI presents and analyzes the RAPS performance based on a moving platform experiment. Section VII concludes the paper and outlines potential directions for future research.

II. GNSS OBSERVATION MODEL

State estimation will be performed using RT-PPP corrected multi-GNSS pseudorange and Doppler measurements. This article focuses on the GNSS constellations that use code division multiple access: GPS, Galileo, and BeiDou.

For each GNSS constellation γ , the single frequency pseudorange observation of satellite s at frequency j tracked by receiver r at time t_r is modeled as [20], [21]

$$\rho_{r,j}^s(t_r) = R(\mathbf{p}_r, \hat{\mathbf{p}}^s) + dt_r^\gamma + M_r^s + \eta_\rho^s - (dt^s - b^s) + T_r^s + I_{r,j}^s + E_r^s \quad (1)$$

where $R(\mathbf{p}_r, \hat{\mathbf{p}}^s) = \|\mathbf{p}_r - \hat{\mathbf{p}}^s\|$ is the geometric range between satellite and receiver, $\hat{\mathbf{p}}^s \in \mathfrak{R}^3$ is the computed satellite position, and $\mathbf{p}_r \in \mathfrak{R}^3$ is the receiver position; dt_r^γ is the receiver clock offset for constellation γ in meters; dt^s is the satellite clock error in meters; b^s is the satellite hardware biases in meters; T_r^s is the tropospheric delay; $I_{r,j}^s$ is the ionospheric delay at j frequency; E_r^s is the ephemeris error in the computed satellite position $\hat{\mathbf{p}}^s$; M_r^s is the multipath error; $\eta_\rho^s \sim \mathcal{N}(0, (\sigma_\rho^s)^2)$ is the pseudorange measurement noise. The hardware biases are normally stable over time [22]. RT-PPP techniques significantly reduce the magnitude of the CME terms. These are listed in the second line of eqn. (1).

After compensating for the satellite velocity and clock drift, which can be computed using ephemeris, the corrected Doppler measurement can be modeled as [7], [23]

$$\delta D_r^s = (\mathbf{1}_r^s)^\top \mathbf{v}_r + \dot{d}t_r + \epsilon_D^s \quad (2)$$

where $\mathbf{v}_r \in \mathbb{R}^3$ is the receiver velocity in meter per second, $\dot{d}t_r$ is the receiver clock drift in meter per second, $\mathbf{1}_r^s$ is the line-of-sight vector from the satellite to the receiver which is defined as

$$\mathbf{1}_r^s = \frac{\mathbf{p}_r - \mathbf{p}^s}{\|\mathbf{p}_r - \mathbf{p}^s\|}, \quad (3)$$

and $\epsilon_{r,D}^s \sim \mathcal{N}(0, (\sigma_D^s)^2)$ is the Doppler measurement noise.

III. REAL-TIME PPP CORRECTIONS

In eqn. (1), without using external corrections, the satellite position and clock error are computed using the broadcast ephemeris, the satellite hardware bias is roughly corrected by timing group delay from the ephemeris, and troposphere and ionosphere are compensated by standard models. This approach yields a range measurement accuracy of about 10 m. RT-PPP corrections for multi-GNSS have been developed and maintained by IGS MGEX with the goal of achieving enhanced accuracy.

TABLE I: Correction sources and models for multi-GNSS single frequency RT-PPP

CME	CME Symbol	Correction sources or models
Satellite orbit and clock	\mathbf{p}^s and dt^s	WHU products [27]
Satellite hardware bias	b^s	CAS GIPP OSB product [25], [28]
Tropospheric delay	T_r^s	IGGtrop [24]
Ionospheric delay	$I_{r,j}^s$	CNES vertical TEC product [29]

This section discusses the choice of RT-PPP corrections used herein to mitigate the CME effects. The PPP corrections are communicated via parameters for models of each component of the CME. They demonstrate efficacy on a global scale. Various sources are available. These sources have been comprehensively defined and examined in [9], [20], [24], [25]. The real-time orbit and clock products are corrections to the satellite position and clock error from broadcast ephemeris. In this study, we choose to use those from WHU. Satellite hardware bias could be corrected using either differential code bias or Observable-specific Code Biases (OSB) format corrections. The multi-GNSS OSB products are more convenient. In this study, the OSB products are provided by CAS. Tropospheric delay is corrected by the global *IGGtrop* empirical model. Ionospheric delay is compensated using the real-time global vertical TEC product provided by CNES. The model and the reasons for choosing it are discussed in Section IV.D of [20]. Table I summarizes the choices.

The RT-PPP corrections related to satellite orbit and clock, satellite hardware bias, and tropospheric delay can achieve centimeter-level accuracy. The assessment of the CNES vertical TEC product indicates that the Root Mean Square (RMS) ranges from 2.07 to 6.15 TEC units, which, when scaled using the GPS L1 frequency, corresponds to 0.34 to 1.00 meters [26].

After mitigating the CMEs, the corrected pseudorange model can be represented as:

$$\delta\rho_r^s(t_r) = R(\mathbf{p}_r, \hat{\mathbf{p}}_c^s) + dt_r^s + M_r^s + \varepsilon_r^s \quad (4)$$

where $\hat{\mathbf{p}}_c^s$ denotes the computed satellite position using the PPP orbit products and $\varepsilon_r^s = \Delta_r^s + \eta_r^s$ where Δ_r^s represents the residual of CMEs.

During the state estimation process, the measurement noise and multipath combined is assumed to be white and normal, $(M_r^s + \varepsilon_r^s) \sim \mathcal{N}(0, (\sigma_\rho^s)^2)$. This is reasonable in open sky conditions where multipath effects are generally small [11], [30]. However, in urban and residential areas, multipath errors can unexpectedly surge to tens of meters. As there's no established model for multipath errors, when they are large, they are treated as outliers. In this study, the variance of pseudorange is computed by $(\sigma_\rho^s)^2 = \sigma_b^2 + (M_a^s \sigma_a)^2 + \sigma_\rho^s$ where σ_b^2 is the variance of PPP corrections excluding ionosphere correction, σ_a^2 is the variance of vertical TEC units of the ionosphere product, and M_a^s is the mapping factor

TABLE II: Standard deviation values for measurement noise model.

σ_b	σ_a	σ_ρ^s	σ_D^s
0.1 m	6.15 TEC	0.9 m	1.414 m/s

(see Sec. 4.5 in [9]) for satellite s . The standard deviation values for the experiment are summarized in Table II.

IV. STATE ESTIMATION

This section describes the state vector and system model. The state vector is defined as

$$\mathbf{x} = [\mathbf{p}_r, \mathbf{v}_r, \mathbf{a}_r, \mathbf{dt}_r, \dot{dt}_r]^\top \in \mathfrak{R}^n \quad (5)$$

where $\mathbf{a}_r \in \mathfrak{R}^3$ denotes the receiver acceleration, $\mathbf{dt}_r \in \mathfrak{R}^{n_s}$ represents the vector of receiver clock offsets for the n_s different constellations, and \dot{dt}_r is the scalar rate of clock offset drift. The state at time $t_k = kT$ will be denoted as \mathbf{x}_k where T is the sampling interval.

The time update portion of the discrete-time model

$$\mathbf{x}_{k+1} = \Phi \mathbf{x}_k + \mathbf{w}_k \quad (6)$$

is a standard position, velocity, acceleration approach where the state transition matrix is

$$\Phi = \begin{bmatrix} \mathbf{I}_3 & T\mathbf{I}_3 & \frac{1}{2}T^2\mathbf{I}_3 & \mathbf{0} & \mathbf{0} \\ \mathbf{0} & \mathbf{I}_3 & T\mathbf{I}_3 & \mathbf{0} & \mathbf{0} \\ \mathbf{0} & \mathbf{0} & \mathbf{I}_3 & \mathbf{0} & \mathbf{0} \\ \mathbf{0} & \mathbf{0} & \mathbf{0} & \mathbf{I}_{n_s} & \mathbf{T}_{n_s} \\ \mathbf{0} & \mathbf{0} & \mathbf{0} & \mathbf{0} & 1 \end{bmatrix} \quad (7)$$

and $\mathbf{w}_k \sim \mathcal{N}(\mathbf{0}, \mathbf{Q})$ is the white Gaussian process noise where the discrete-time process noise covariance matrix \mathbf{Q} can be computed from the continuous-time power spectral density using eqn. (4.110) in [7], \mathbf{I}_q represents the identity matrix of dimension q , and \mathbf{T}_{n_s} is a column vector with n_s elements all having value of T . The symbol $\mathbf{0}$ is a conformal matrix containing all zeros.

The measurement vector at time k is:

$$\mathbf{y}_k = \mathbf{h}(\mathbf{x}_k) + \boldsymbol{\epsilon}_k \quad (8)$$

where $\mathbf{y}_k = [\delta\rho_r^1, \dots, \delta\rho_r^m, \delta D_r^1, \dots, \delta D_r^m]^\top \in \mathfrak{R}^{2m}$ contains corrected pseudorange and Doppler measurements for m satellites, $\mathbf{h}(\mathbf{x}_k) = [h_\rho^1(x_k), \dots, h_\rho^m(x_k), h_D^1(x_k), \dots, h_D^m(x_k)]^\top$ represents the measurement models where

$$h_\rho^m(\mathbf{x}_k) = R(\mathbf{p}_r, \mathbf{p}_c^s) + c dt_r^s \text{ and} \\ h_D^m(\mathbf{x}_k) = (\mathbf{1}_r^s)^\top \cdot \mathbf{v}_r + c \dot{dt}_r,$$

and $\boldsymbol{\epsilon}_k \sim \mathcal{N}(\mathbf{0}, \mathbf{R}_k)$ represents the Gaussian measurement noise. The pseudorange and Doppler measurement noises are mutually uncorrected, each is white, and both are uncorrelated between satellites; therefore, the covariance matrix $\mathbf{R}_k = \text{diag}([\sigma_\rho^1]^2, \dots, \sigma_\rho^m)^2, (\sigma_D^1)^2, \dots, (\sigma_D^m)^2])$ is diagonal and invertible.

The time propagation model for the state estimate is:

$$\hat{\mathbf{x}}_{k+1}^- = \Phi \hat{\mathbf{x}}_k^+, \quad (9)$$

$$\mathbf{P}_{k+1}^- = \Phi \mathbf{P}_k^+ \Phi^\top + \mathbf{Q} \quad (10)$$

where $\hat{\mathbf{x}}_k^-$ and $\hat{\mathbf{x}}_k^+$ denote the prior and posterior state estimate, and \mathbf{P}_k^- and \mathbf{P}_k^+ denote the prior and posterior state estimate error covariance matrix. The Probability Density Function (PDF) of prior state \mathbf{x}_k is assumed to be Gaussian $\mathbf{x}_k \sim \mathcal{N}(\hat{\mathbf{x}}_k^-, \mathbf{P}_k^-)$. Outliers are not directly involved in the time propagation process since they only affect the measurements, the outlier accommodation is considered in the measurement update process.

V. MEASUREMENT OUTLIER ACCOMMODATION

This section reviews the traditional TD outlier rejection approach and presents RAPS estimation [18] modified for the diagonal performance specification constraint.

Measurement selection will be implemented by use of a vector $\mathbf{b} = [b_1, \dots, b_{2m}]^\top$ with $b_i \in \{0, 1\}$, see [31]. The vector \mathbf{b} is used to select a certain measurement to be used ($b_i = 1$) in the measurement update or to be ignored ($b_i = 0$). The maximum-a-posteriori state estimation, for a fixed value of \mathbf{b} , yields the nonlinear least squares problem

$$\hat{\mathbf{x}}_k^+ = \underset{\mathbf{x}_k}{\operatorname{argmin}} C(\mathbf{x}_k, \mathbf{b}) \quad (11)$$

where the cost function (see [18])

$$\begin{aligned} C(\mathbf{x}_k, \mathbf{b}) &= \|\Sigma_{\mathbf{P}}(\mathbf{x}_k - \hat{\mathbf{x}}_k^-)\|^2 + \|\Sigma_{\mathbf{R}} \Psi(\mathbf{b})(\mathbf{h}(\mathbf{x}_k) - \mathbf{y}_k)\|^2 \\ &= \|\Sigma_{\mathbf{P}}(\mathbf{x}_k - \hat{\mathbf{x}}_k^-)\|^2 + \sum_{i=1}^{2m} \frac{b_i^2}{\sigma_i^2} \mathbf{e}_i \mathbf{e}_i^\top (\mathbf{h}(\mathbf{x}_k) - \mathbf{y}_k)^2 \\ &= \|\Sigma_{\mathbf{P}}(\mathbf{x}_k - \hat{\mathbf{x}}_k^-)\|^2 + \sum_{i=1}^{2m} \frac{b_i}{\sigma_i^2} \mathbf{e}_i \mathbf{e}_i^\top (\mathbf{h}(\mathbf{x}_k) - \mathbf{y}_k)^2 \end{aligned}$$

where $b_i^2 = b_i$, $\Psi(\mathbf{b}) = \operatorname{diag}(\mathbf{b})$, $\Sigma_{\mathbf{R}}^\top \Sigma_{\mathbf{R}} = \mathbf{R}_k^{-1}$, $\Sigma_{\mathbf{P}}^\top \Sigma_{\mathbf{P}} = (\mathbf{P}_k^-)^{-1}$, σ_i^2 is the i -th diagonal element of \mathbf{R}_k , and \mathbf{e}_i is the i -th standard basis vector. For any fixed value of \mathbf{b} , the minimum of $C(\mathbf{x}_k, \mathbf{b})$ as a function of \mathbf{x}_k quantifies the risk associated with the measurements selected by \mathbf{b} .

The posterior information matrix, when using the measurements selected by \mathbf{b} , is:

$$\begin{aligned} \mathbf{J}_b^+ &= \mathbf{H}^\top \Psi(\mathbf{b})^\top \mathbf{R}^{-1} \Psi(\mathbf{b}) \mathbf{H} + \mathbf{J}_k^- \\ &= \sum_{i=1}^{2m} \frac{b_i}{\sigma_i^2} \mathbf{h}_i^\top \mathbf{h}_i + \mathbf{J}_k^- \end{aligned} \quad (12)$$

where \mathbf{h}_i is the i -th row of $\mathbf{H} = \frac{\partial}{\partial \mathbf{x}} \mathbf{h}(\mathbf{x})|_{\mathbf{x}=\mathbf{x}_k} \in \mathbb{R}^{2m \times n}$ and $\mathbf{J}_k^- = (\mathbf{P}_k^-)^{-1}$ is the prior information matrix. The corresponding posterior covariance matrix is $\mathbf{P}_k^+ = (\mathbf{J}_b^+)^{-1}$.

Two strategies are considered for determining \mathbf{b} .

A. Threshold Decisions

The traditional approach for detecting and removing outliers in state estimation employs a threshold test on each scalar measurement residual. The vector of residuals is computed as

$$\mathbf{r}_k = \mathbf{y}_k - \mathbf{h}(\hat{\mathbf{x}}_k^-). \quad (13)$$

Let r_i denote the i -th element of \mathbf{r}_k . The selection of \mathbf{b} is determined by

$$b_i = \begin{cases} 0, & \text{when } |r_i| \geq \lambda \sigma_{r_i} \\ 1, & \text{when } |r_i| < \lambda \sigma_{r_i} \end{cases} \quad (14)$$

where $\lambda > 0$ is the decision threshold and $\sigma_{r_i}^2 = \mathbf{h}_i \mathbf{P}_k^- \mathbf{h}_i^\top + \sigma_i^2$ is the covariance of r_i (see e.g., [12]–[14]). For the selection vector \mathbf{b} that results, the optimal estimate $\hat{\mathbf{x}}_k^+$ and its posterior information \mathbf{J}_b^+ are the solutions of eqn. (11) and eqn. (12).

The threshold test approach requires the designer to select a decision threshold λ . Regardless of the existence of outliers, \mathbf{J}_b^+ is maximized by selecting all measurements, which would be fine if no outliers existed. When outliers exist, the state estimate and error covariance matrix are only correct when all outliers are removed at each epoch. However, in practice, no detection method is flawless. Missed outlier detection corrupts the state estimate mean $\hat{\mathbf{x}}_k^+$ and causes the covariance matrix to underestimate the true uncertainty. This leads to an inconsistency between the mean and variance, rendering subsequent outlier decisions unreliable. Moreover, the TD approach has a fixed decision criteria that makes decisions without regard to the performance specification.

B. RAPS Approach

Instead of focusing on detecting outliers, RAPS seeks to select a subset of measurements to use that minimize the risk, as quantified by $C(\mathbf{x}_k, \mathbf{b})$, while achieving the defined accuracy specification. This accuracy specification is realized by imposing a constraint on the posterior information matrix within an optimization framework. The previous research in [17], [18] employed a semi-definite matrix constraint (i.e., $\mathbf{J}_b^+ \geq \Psi(\mathbf{J}_d)$). Herein, we consider an alternative diagonal performance constraint. Use of the diagonal constraint reduces the computational cost of the optimization. This formulation has not been evaluated in the literature previously. Moreover, earlier studies mainly analyzed the impact on positioning performance as a function of outlier magnitudes by artificially imposing outliers. The efficacy of RAPS is particularly intriguing in the context of real-world RT-PPP applications.

The RAPS optimization problem, utilizing the diagonal performance specification, is expressed as:

$$\left. \begin{aligned} \mathbf{x}_k^+, \mathbf{b}^* &= \underset{\mathbf{x}_k, \mathbf{b}}{\operatorname{argmin}} C(\mathbf{x}_k, \mathbf{b}) \\ \text{s.t.: } & \operatorname{diag}(\mathbf{J}_b^+) \geq \mathbf{J}_d \\ & b_i \in \{0, 1\} \text{ for } i = 1, \dots, 2m \end{aligned} \right\} \quad (15)$$

where \mathbf{J}_d represents a positive vector defining the performance constraint for each element of the state vector. The user-defined performance constraint parameter \mathbf{J}_d to achieve the SAE J2945 is discussed in Section III-B of [17]. The parameters to achieve this specification are defined by

$$\mathbf{J}_p = [1.929, 1.929, 0.121]^\top \text{ and } \mathbf{J}_v = [1.389, 1.389, 0.347]^\top$$

with $\mathbf{J}_d = [\mathbf{J}_p^\top, \mathbf{J}_v^\top]^\top$. The first two elements of \mathbf{J}_p and \mathbf{J}_v specify the local tangent plane north and east direction information bounds, while the third element applies to the vertical direction.

Starting from eqn. (12), the constraint $\text{diag}(\mathbf{J}_b^+) \geq \mathbf{J}_d$ can be expressed as

$$\sum_{2m}^{i=1} \frac{b_i}{\sigma_i^2} \text{diag}(\mathbf{h}_i^\top \mathbf{h}_i) + \text{diag}(\mathbf{J}_k^-) \geq \mathbf{J}_d. \quad (16)$$

The solution to the RAPS optimization problem for the matrix constraint $\mathbf{J}_b^+ \geq \Psi(\mathbf{J}_d)$ is discussed in [17]. This case requires a positive definiteness check on $(\mathbf{J}_b^+ - \Psi(\mathbf{J}_d))$, which is an $O(n^3)$ computation. The solution in [17] employed an exhaustive search strategy for the binary vector \mathbf{b} , which has computational cost $O(m!)$. In contrast, the diagonal case in eqn. (16) only requires n scalar inequality evaluations. An efficient solution to Problem (15), using a block coordinate method with polynomial time-complexity, is described in Sec. 6 of [32] and is utilized in this paper.

VI. EXPERIMENT PERFORMANCE AND ANALYSIS

This section presents experimental results for the GNSS positioning using RAPS and RT-PPP corrections. Results from TD, RAPS, and the standard Extended Kalman Filter (EKF) are compared. To be comparable with automotive applications, a low-cost u-blox F9P receiver is used to acquire the raw GNSS measurements on a moving platform. The analysis of multi-GNSS RT-PPP is performed using GPS L1, Galileo E1, and Beidou B1 signals. The elevation cut-off is 10 degrees. The experimental vehicle navigated through urban and residential zones near University of California, Riverside, traversing areas characterized by narrow lanes with tall trees lining the road. Throughout the experiment, the u-blox maintained communication with a nearby base station. The *ground truth* trajectory was established using u-blox’s native multi-GNSS, dual-frequency, integer-fixed RTK solution to achieve centimeter accuracy.¹

A. Estimators

The results are compared for three estimators. The time propagation for all estimators is identical. The measurement update for all estimators determines the posterior state \mathbf{x}_k^+ by minimizing the cost function in eqn. (11), but choose \mathbf{b} differently.

EKF: Uses all measurements (i.e., $\mathbf{b} = \mathbf{1}$). Since it uses all measurements both the cost and the posterior information matrix will be maximized over all choices of \mathbf{b} .

TD: Defines \mathbf{b} using eqn. (14) with $\lambda = 1.5$.

RAPS: Chooses \mathbf{b} during the solution of the optimization problem to satisfy the performance specification constraint, as stated in eqn. (15).

B. Metrics

The analysis of positioning performance between different estimators will be based on the following metrics:

- North, East and Down frame coordinate errors: $\delta p_N, \delta p_E, \delta p_D$;
- Horizontal positioning error: $HE = \sqrt{\delta p_N^2 + \delta p_E^2}$;

¹The experiment code is public on GitHub: github.com/Azurehappen/Outlier_Accommodation_GNSS_ACC2

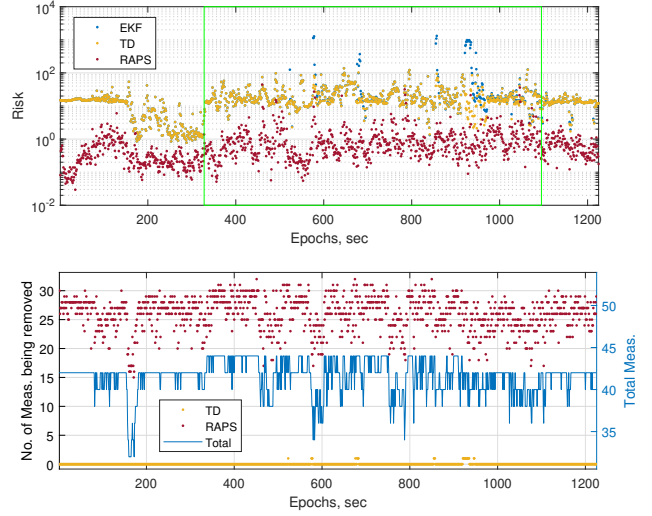


Fig. 1: The top graphs display experimental results for the risk from EKF in blue, EKF with TD in orange, and RAPS in red. The solid green box indicates the period during which the driving was under non-clear view of sky conditions. The bottom graphs display the number of measurements removed by either RAPS or TD (left y-axis) and the total number of measurements available (right y-axis). The number of measurements available is equivalent to the number used by the EKF.

- Vertical positioning error: $VE = |\delta p_D|$; and
- Estimation risk as quantified by $C(\mathbf{x}_k^+, \mathbf{b})$.

C. Results

The performance of the three estimators is evaluated based on their estimation risk and positioning accuracy. The top graphs in Fig. 1 display the risks across all epochs. The time period highlighted by the green box represents the vehicle’s journey through the residential areas, in which the narrow lanes with tall trees increase the probability of encountering frequent and significant outlier measurements. This time period is referred to as the “obstructed view” condition. In contrast, other epochs offer a clear view of the open sky.

The red graph indicates that RAPS consistently achieves the lowest risk. Both EKF and TD exhibit risks that are significantly higher than that of RAPS. In many epochs, the risk difference between EKF and TD is small, so the EKF data is covered by the TD data. This shows that for most time epochs, most residuals passed the TD test, even with the reasonable small value of λ , regardless of whether the conditions were open sky or not. Notably, during specific epochs (around 600s and 1000s), EKF demonstrates a pronounced risk, whereas TD exhibits a reduced risk due to its ability to reject severe outliers.

The bottom graphs in Fig. 1 display the number of measurements discarded by RAPS or TD. RAPS selects a subset of measurements to minimize risk while achieving the performance specifications. The solution is feasible for all epochs, even while removing many more measurements

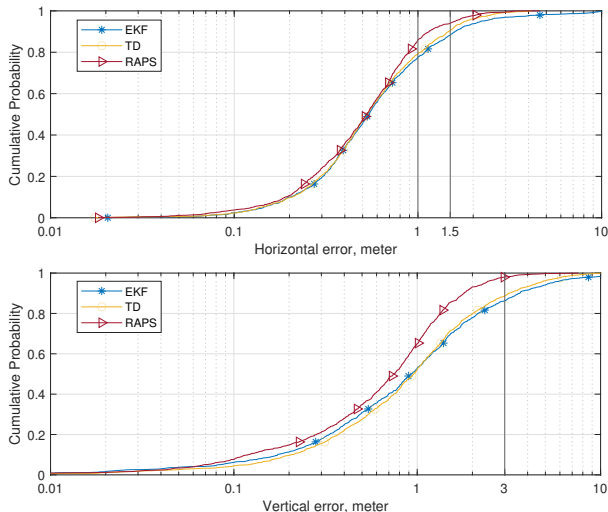


Fig. 2: The cumulative error distribution of horizontal (top figure) and vertical (bottom figure) positioning errors for EKF in blue, EKF with TD in orange, and RAPS in red for the entire experiment trajectory.

than TD. At each epoch, RAPS adapts both the number of satellites removed and the specific satellites removed based on the number and geometry of the available measurements as well as their specific residuals. This selection results in the reduced risk demonstrated in the top figure while achieving the performance specification at all times.

Fig. 2 presents the cumulative probability distribution for both horizontal and vertical positioning errors, using a consistent color scheme with Fig. 1. Table III and IV provide a summary of the positioning performance statistics from the different estimators under various conditions. Table III includes the mean, RMS, and maximum values of the norm and absolute value of the horizontal and vertical errors. Table III displays the probability of the positioning errors being less than the specified threshold corresponding to the SAE specification. The best results are highlighted in bold. Throughout the entire experimental period, RAPS delivers superior results, with the exception of the maximum horizontal error, which exceeds that of TD by 0.39 m. RAPS showcases an advantage of approximately 3.51-12% across all probability metrics. It is notable that all maximum errors originate from the non-clear sky condition. Segmenting the comparison between non-clear sky and open sky conditions, single frequency RT-PPP performance of these three estimators all surpass the SAE requirements under both conditions. Further analysis is as follows:

- Obstructed View: RAPS enhances the horizontal accuracy at both 1-meter and 1.5-meter levels by approximately 6-12% compared to TD. While TD outperforms EKF, the improvements are relatively smaller. TD struggles to eliminate sufficient outliers for better performance. Its inability to detect certain outliers results in close risks comparable to those of EKF, as depicted in Fig. 1. In this sky condition, RAPS achieves the lowest

		Mean (m)	RMS (m)	Max (m)
		HE / VE	HE / VE	HE / VE
Overall	EKF	0.87 / 1.58	1.52 / 2.617	12.39 / 20.19
	TD	0.70 / 1.39	0.91 / 2.03	4.12 / 10.54
	RAPS	0.63 / 0.90	0.80 / 1.19	4.61 / 7.57
Obstructed View	EKF	1.14 / 2.09	1.88 / 3.29	12.39 / 20.19
	TD	0.88 / 1.75	1.08 / 2.46	4.12 / 10.54
	RAPS	0.73 / 0.95	0.90 / 1.28	4.61 / 7.57
Open sky	EKF	0.41 / 0.75	0.49 / 0.96	2.59 / 4.81
	TD	0.41 / 0.78	0.50 / 0.98	2.59 / 4.81
	RAPS	0.48 / 0.80	0.58 / 1.03	2.13 / 4.89

TABLE III: Horizontal and vertical position error magnitudes.

		Prob. of HE \leq 1.0 m	Prob. of HE \leq 1.5 m	Prob. of VE \leq 3.0 m
Overall	EKF	77.55%	88.24%	86.12%
	TD	79.76%	90.86%	88.65%
	RAPS	86.04%	93.96%	98.12%
Obstructed View	EKF	66.27%	81.83%	78.30%
	TD	69.80%	86.01%	82.48%
	RAPS	82.09%	91.63%	97.52%
Open sky	EKF	96.03%	98.91%	99.13%
	TD	96.30%	98.91%	98.91%
	RAPS	92.61%	97.83%	99.13%

TABLE IV: Horizontal and vertical position error probabilities.

mean and RMS. Both TD and RAPS exhibit fewer and smaller maximum positioning errors in challenging scenarios compared to EKF.

- Open sky: The performance disparities among the three estimators are less pronounced under open sky conditions, which typically present minimal outliers. If it were known that there were no outliers and the goal was to minimize state estimation error, then using all measurements is the correct approach, which is what the EKF is doing. When the goal is to achieve a state specification, then using all measurements invokes extra risk. RAPS will only use the best set of measurements to achieve the specification at the lowest risk. Therefore, RAPS is not designed to lead in statistical performance under open sky (no outlier) conditions, yet it does comparably well by minimizing risk subject to its performance constraint. Because both EKF and TD use essentially all measurements, their posterior state and error covariance remain similar to each other. Also, both their risk and (theoretical) posterior information will be higher than that of RAPS.

VII. CONCLUSION AND DISCUSSION

This paper presents, implements, and demonstrates the diagonal specification RAPS approach for outlier accommodation with a focus on GNSS single frequency applications using RT-PPP correction information. EKF, traditional TD,

and RAPS approaches are evaluated and compared. All estimators have the option to select from the same GNSS pseudorange and Doppler measurements to use at each epoch. Each algorithm makes different choices resulting in different risk and performance. The experimental data set include both open sky and obstructed view conditions. The results demonstrate that all three approaches achieve performance that exceeds the SAE specification when averaged over the entire data set. In challenging time intervals with obstructed views or heightened multipath effects, the RAPS approach, using diagonal performance specification constraints, outperforms the rest. It shows improvements of 6-12% over TD and 10-19% over EKF.

Several avenues can be explored in future research. The extension to carrier-phase measurements would be valuable for enhanced precision. However, leveraging carrier-phase measurements in a single frequency context is challenging to to inaccuracy in the ionospheric PPP products, whose accuracy may be enhanced with the launch of Stage 3 of IGS schedule for the near future [9]. Multi-frequency scenarios are also of interest for addressing the ionospheric delay to make carrier phase feasible in life-critical applications.

VIII. ACKNOWLEDGMENT

The authors gratefully acknowledge the UCR KA Endowment and the US DOT CARNATIONS Center, each of which has provided partial funding for this research.

The ideas reported herein, and any errors or omissions, are the responsibility of the authors and do not reflect the opinions of the sponsors.

REFERENCES

- [1] N. Williams, P. B. Darian, G. Wu, P. Closas, and M. Barth, "Impact of Positioning Uncertainty on Connected and Automated Vehicle Applications," *SAE Inter. J. of Connected and Automated Vehicles*, vol. 6, no. 12-06-02-0010, 2022.
- [2] J. A. Farrell, G. Wu, W. Hu, D. Oswald, and P. Hao, "Lane-Level Localization and Map Matching for Advanced Connected and Automated Vehicle (CAV) Applications," *National Center for Sustainable Transportation (NCST) (UTC)*, 2023. [Online]. Available: <https://doi.org/10.7922/G25T3HSS>
- [3] H. Xia, K. Boriboonsomsin, and M. Barth, "Indirect Network-Wide Energy/Emissions Benefits from Dynamic Eco-Driving on Signalized Corridors," in *14th Int. IEEE ITSC*, 2011, pp. 329–334.
- [4] Z. Yu, Y. Hu, and J. Huang, "GPS/INS/Odometer/DR integrated navigation system aided with vehicular dynamic characteristics for autonomous vehicle application," *IFAC-PapersOnLine*, vol. 51, no. 31, pp. 936–942, 2018.
- [5] Anonymous. (March 2016) On-Board System Requirements for V2V Safety Communications. [Online]. Available: https://www.sae.org/standards/content/j2945/1_201603/
- [6] GPS Product Team, "Global Positioning System Standard Positioning Service Performance Analysis Report," *GPS Product Team: Washington, DC, USA*, 2020. [Online]. Available: https://www.nstb.tc.faa.gov/reports/2020_Q4_SPS_PAN_v2.0.pdf
- [7] J. A. Farrell, *Aided Navigation: GPS with High Rate Sensors*. McGraw-Hill, Inc., 2008.
- [8] P. Teunissen and O. Montenbruck, *Springer Handbook of Global Navigation Satellite Systems*. Springer, 2017.
- [9] International GNSS Service, "IGS State Space Representation (SSR) Format Version 1.00," *IGS Real-Time Working Group*, 2020.
- [10] F. O. Silva, W. Hu, and J. A. Farrell, "Real-Time Single-Frequency Precise Point Positioning for Connected Autonomous Vehicles: A Case Study Over Brazilian Territory," in *22nd IFAC World Congress*, vol. 56, no. 2, 2023, pp. 5703–5710.
- [11] J.-B. Uwineza, F. Rahman, F. Silva, W. Hu, and J. A. Farrell, "Characterizing GNSS Multipath at Different Antenna Mounting Positions on Vehicles," *UC Riverside: Bourns College of Engineering*, 2019. [Online]. Available: <https://escholarship.org/uc/item/9nj3459s>
- [12] R. A. Fisher, "Statistical Methods for Research Workers," in *Breakthroughs in Statistics*. Springer, 1992, pp. 66–70.
- [13] P. M. Frank and X. Ding, "Survey of Robust Residual Generation and Evaluation Methods in Observer-Based Fault Detection Systems," *J. of Process Control*, vol. 7, pp. 403–424, 1997.
- [14] R. J. Patton and J. Chen, "A review of parity space approaches to fault diagnosis," *IFAC Proceedings Volumes*, vol. 24, no. 6, pp. 65–81, 1991.
- [15] D. Wang, H. Lu, and M.-H. Yang, "Robust visual tracking via least soft-threshold squares," *IEEE T-CSVT*, vol. 26, no. 9, pp. 1709–1721, 2015.
- [16] P. J. Rousseeuw, "Least Median of Squares Regression," *J. of the American Statistical Association*, vol. 79, no. 388, pp. 871–880, 1984.
- [17] E. Aghapour, F. Rahman, and J. A. Farrell, "Outlier accommodation in nonlinear state estimation: A risk-averse performance-specified approach," *IEEE T-CST*, pp. 1–13, 2019.
- [18] E. Aghapour, F. Rahman, and J. A. Farrell, "Outlier Accommodation for Meter-Level Positioning: Risk-Averse Performance-Specified State Sstimation," in *IEEE/ION PLANS*, 2018, pp. 627–633.
- [19] F. Rahman, E. Aghapour, and J. A. Farrell, "Outlier Accommodation by Risk-Averse Performance-Specified Nonlinear State Estimation: GNSS Aided INS," in *IEEE CDC*, 2018, pp. 5922–5927.
- [20] W. Hu, A. Neupane, and J. A. Farrell, "Using PPP Information to Implement a Global Real-Time Virtual Network DGNSS Approach," *IEEE T-VT*, vol. 71, no. 10, pp. 10 337–10 349, 2022.
- [21] X. Li, M. Ge, X. Dai, X. Ren, M. Fritsche, J. Wickert, and H. Schuh, "Accuracy and Reliability of Multi-GNSS Real-time Precise Positioning: GPS, GLONASS, BeiDou, and Galileo," *J. of Geodesy*, vol. 89, no. 6, pp. 607–635, 2015.
- [22] E. Sardon, A. Rius, and N. Zarraoa, "Estimation of the Transmitter and Receiver Differential Biases and the Ionospheric Total Electron Content from Global Positioning System Observations," *Radio science*, vol. 29, no. 03, pp. 577–586, 1994.
- [23] F. Rahman, E. Aghapour, and J. Farrell, "ECEF Position Accuracy and Reliability in the Presence of Differential Correction Latency Year 1 Technical Report for Sirius XM," *UC Riverside: Bourns College of Engineering*, 2018. [Online]. Available: <https://escholarship.org/uc/item/38d3h08w>
- [24] W. Li, Y. Yuan, J. Ou, H. Li, and Z. Li, "A New Global Zenith Tropospheric Delay Model IGGtrop for GNSS Applications," *Chinese Science Bulletin*, vol. 57, no. 17, pp. 2132–2139, 2012.
- [25] S. Schaer, "SINEX BIAS—Solution (Software/Technique) Independent Exchange Format for GNSS Biases Version 1.00," in *IGS Workshop on GNSS Biases, Bern, Switzerland*, 2016.
- [26] Z. Nie, H. Yang, P. Zhou, Y. Gao, and Z. Wang, "Quality Assessment of CNES Real-time Ionospheric Products," *GPS Solutions*, vol. 23, pp. 1–15, 2019.
- [27] J. Guo, X. Xu, Q. Zhao, and J. Liu, "Precise Orbit Determination for Quad-Constellation Satellites at Wuhan University: Strategy, Result Validation, and Comparison," *J. of Geodesy*, vol. 90, pp. 143–159, 2016.
- [28] N. Wang, Z. Li, B. Duan, U. Hugentobler, and L. Wang, "GPS and GLONASS Observable-Specific Code Bias Estimation: Comparison of Solutions from the IGS and MGEX Networks," *J. of Geodesy*, vol. 94, no. 8, pp. 1–15, 2020.
- [29] D. Roma-Dollase, M. Hernández-Pajares, A. García-Rigo, D. Laurichesse, M. Schmidt, E. Erdogan, Y. Yuan, Z. Li, J. M. Gómez-Cama, A. Krankowski *et al.*, "Real Time Global Ionospheric Maps: a Low Latency Alternative to Traditional GIMs," *Radio Science*, vol. 47, no. 0, 2016.
- [30] S. Khanafseh, B. Kujur, M. Joerger, T. Walter, S. Pullen, J. Blanch, K. Doherty, L. Norman, L. de Groot, and B. Pervan, "GNSS Multipath Error Modeling for Automotive Applications," in *Proc. of ION GNSS+*, 2018, pp. 1573–1589.
- [31] L. Carlone, A. Censi, and F. Dellaert, "Selecting Good Measurements via ℓ_1 Relaxation: A Convex Approach for Robust Estimation over Graphs," in *2014 IEEE/RSJ Inter. Conf. on Intelligent Robots and Systems*, 2014, pp. 2667–2674.
- [32] W. Hu, "Optimization-Based Risk-Averse Outlier Accommodation With Linear Performance Constraints: Real-Time Computation and Constraint Feasibility in CAV State Estimation," *UC Riverside*, 2024. [Online]. Available: <https://escholarship.org/uc/item/5mf54016>